Tapioca starch in the sol-gel synthesis of cobalt ferrites with divalent cation substitutions

Anuchit Hunyek
Program of General Education - Science (Physics), Faculty of Liberal Arts, Rajamangala University of Technology Rattanakosin,

Chitnarong Sirisathitkul
School of Science and Center of Excellence in Functional Materials and Nanotechnology, Walailak University

Krit Koyvanich
Department of Physics, Prince of Songkla University, 5610230001@email.psu.ac.th

University of **Kerbala**

Tapioca starch in the sol-gel synthesis of cobalt ferrites with divalent cation substitutions

Abstract

An aqueous solution of tapioca starch was successfully used as a chelating agent in the sol-gel synthesis of $Co_{0.7}Me_{0.3}Fe_2O_4$, where Me denotes Co, Mn, Cu, Ni, or Zn. The hysteresis loops of all sintered ferrites revealed ferrimagnetic properties. The saturation magnetization was reduced in $Co_{0.7}Cu_{0.3}Fe_2O_4$ and $Co_{0.7}Ni_{0.3}Fe_2O_4$ because of the ion substitutions with smaller magnetic moments. Interestingly, $Co_{0.7}Cu_{0.3}Fe_2O_4$ exhibited the highest saturation magnetization and the lowest coercive field. This result demonstrates the value addition of local agricultural products in controlling nanoparticle formation during sol-gel synthesis.

Keywords

Cobalt ferrite; Nanoparticles; Sol-gel reaction; Tapioca starch; Ion substitution

Creative Commons License

RESEARCH PAPER

Tapioca Starch in the Sol−gel Synthesis of Cobalt Ferrites with Divalent Cation Substitutions

Anuchit Hunyek [a], Chitnarong Sirisathitkul [b], Krit Koyvanich [c,*]

[a] Program of General Education - Science (Physics), Faculty of Liberal Arts, Rajamangala University of Technology Rattanakosin, Wangkaikangwon Campus, Prachuap Khiri Khan, Thailand
[b] School of Science and Center of Excellence in Functional Materials and Nanotechnology, Walailak University, Nakhon Si Thammarat, Thailand
[c] Department of Physics, Prince of Songkla University, Songkhla, Thailand

Abstract

An aqueous solution of tapioca starch was successfully used as a chelating agent in the sol−gel synthesis of $Co_{0.7}Me_{0.3}Fe_2O_4$, where Me denotes Co, Mn, Cu, Ni, or Zn. The hysteresis loops of all sintered ferrites revealed ferrimagnetic properties. The saturation magnetization was reduced in $Co_{0.7}Cu_{0.3}Fe_2O_4$ and $Co_{0.7}Ni_{0.3}Fe_2O_4$ because of the ion substitutions with smaller magnetic moments. Interestingly, $Co_{0.7}Cu_{0.3}Fe_2O_4$ exhibited the highest saturation magnetization and the lowest coercive field. This result demonstrates the value addition of local agricultural products in controlling nanoparticle formation during sol−gel synthesis.

Keywords: Cobalt ferrite, Nanoparticles, Sol−gel reaction, Tapioca starch, Ion substitution

1. Introduction

The versatility of cobalt ferrite ($CoFe_2O_4$) has been demonstrated in electromagnetic, environmental, and biomedical applications [1−3]. It belongs to the class of spinel ferrites denoted as AB_2O_4, where A^{2+} is a divalent cation (such as Co^{2+}, Fe^{2+}, Mn^{2+}, Ni^{2+}, Cu^{2+}, and Zn^{2+}) and trivalent B^{3+} is an Fe^{3+} ion. The cubic close-packed structure arranges 32 oxide anions (O^{2-}) in a unit cell with 8 tetrahedral (A_{tet}) and 16 octahedral (B_{oct}) occupied sites. Zinc ferrite ($ZnFe_2O_4$) has a typical spinel structure with all divalent cations (A^{2+}) on the A_{tet}-site and trivalent cations (B^{3+}) on the B_{oct}-sites [4]. The inverse spinel is a configuration with divalent cations (A^{2+}) on the B_{oct}-sites and evenly distributed trivalent cations (B^{3+}) between the A_{tet}-site and B_{oct}-site as observed in $CoFe_2O_4$: $[Fe^{3+}_{tet}(Co^{2+}, Fe^{3+})_{oct}O_4]$ and nickel ferrite ($NiFe_2O_4$): $(Fe^{3+}_{tet}(Ni^{2+}, Fe^{3+})_{oct}O_4)$ [5]. The different magnetic moments of the cations distributed at the A_{tet}-site and B_{oct}-site give particular characteristics to the ferrites. Variations in divalent or trivalent cations tend to alter their magnetic and electric properties.

Microemulsion [6], microwave-assisted synthesis [7], and polymerized complex methods [8] are among the various techniques available for preparing nanoparticles. Chemical co-precipitation and sol−gel syntheses use aqueous solution mixing as a facile route for mass production. The sol−gel method is beneficial for formulating ferrite thin films [9] and nanocomposites [10], as well as substituting other metal or alkaline ions in ferrites [11]. Precursors decompose in situ nanoparticle formation during the gel reaction. The chelating agent effectively controlled the growth of crystals during nanoparticle formation and was conveniently removed during the thermal treatment phase. Therefore, the molecular homogeneity of single-phase nanoparticles can be controlled [12].

Conventional chemical uses, including oleic and citric acids as surfactants in−the sol−gel synthesis, are not environmentally friendly. The chemicals have been replaced and reduced in several green

* Corresponding author.
E-mail address: 5610230001@email.psu.ac.th (K. Koyvanich).

syntheses [13,14]. For $CoFe_2O_4$ synthesis, bioorganic substances are convenient for temperature control [15], and effective with other additives in the sol–gel reaction [16]. Ion substitution in $CoFe_2O_4$ modifies the magnetic characteristics via preferential site occupancy and particle size, such that the materials are suitable for sensing or biomedical applications [17]. The introduction of a transition metal with a smaller ionic radius, such as Ni^{2+}, decreases the coercive field to a value applicable for high-density data storage [18].

The sol–gel method in this study utilizes tapioca starch to synthesize pristine $CoFe_2O_4$ and $Co_{0.7}Me_{0.3}Fe_2O_4$, where Me denotes ion substitution by zinc (Zn), nickel (Ni), copper (Cu), and manganese (Mn). Tapioca starch is abundant in several regions of the world. As demonstrated in [19–21], its utilization for controlling nanoparticle formation is highly advantageous. It is anticipated that structural and magnetic parameters of ferrites obtained from this tapioca starch-assisted sol–gel synthesis will stimulate the replacement of toxic chemicals with this environmentally benign chelating agent in commercial processes, which also adds value to the local tapioca industry.

2. Materials and methods

2.1. Synthesis

Tapioca starch was slowly added to stirring distilled water (15% weight/volume) and kept at 70–80 °C until its viscosity was significantly increased. Iron nitrate $(Fe(NO_3)_3 \cdot 9H_2O)$ and cobalt nitrate $(Co(NO_3)_2 \cdot 6H_2O)$ powders were mixed with a solution of tapioca starch in a w/v ratio of 2:1:36. Carbohydrates in the solution were broken down into several glucose molecules and acted as chelating agents in the nanoparticle synthesis, as schematically shown in Fig. 1. To substitute ions, $Co(NO_3)_2 \cdot 6H_2O$ and $Fe(NO_3)_3 \cdot 6H_2O$ were mixed with one of the following precursors: zinc nitrate

$(Zn(NO_3)_2 \cdot 6H_2O)$, nickel nitrate $(Ni(NO_3)_2 \cdot 6H_2O)$, copper nitrate $(Cu(NO_3)_2 \cdot 3H_2O)$, or manganese nitrate $(Mn(NO_3)_2 \cdot 6H_2O)$. The mixed powder was dissolved in an aqueous solution of tapioca starch. The solution was stirred at 80 °C until it became a gel. Finally, all the sol–gel-derived products were sintered at 800 °C for 4 h to enhance their crystallinity [22].

2.2. Characterization

The decomposition and oxidation states of the chelating agent were studied using thermogravimetric analysis (TGA; PerkinElmer TGA7) in the range of 100–1000 °C to determine the appropriate thermal treatment conditions for the sol–gel derived products. Functional groups in the sintered ferrites were detected by Fourier-transform infrared spectroscopy (FT-IR; PerkinElmer LR 64912C) from 400 to 4000 cm^{-1} at a scanning rate of 40 steps/min. Morphology analysis was performed using field-emission scanning electron microscopy (FE-SEM; Carl Zeiss Model Auriga). The average particle sizes were obtained from the micrographs.

The crystallographic structures of the sintered ferrites were identified by powder X-ray diffractometry (XRD; Rigaku TTRAXIII) using a Cu Kα X-ray of 1.54058 Å. The 2θ angle in the measurement was varied from 10 to 70° with a rotating step of 0.02°/s. The lattice constant (*a*) was determined from the XRD data as follows:

$$a = d_{hkl}\sqrt{h+k+l}, \tag{1}$$

where *d* and (*h, k, l*) denote the interplanar distance and Miller index, respectively [23]. The Nelson–Riley plot of the calculated values of *a* for different phases is plotted against the error function $f(\theta)$ in Eq. (2) [24], corrected by the lattice constant *a*.

$$f(\theta) = \frac{1}{2}\left(\frac{\cos^2\theta}{\sin\theta} + \frac{\cos^2\theta}{\theta}\right), \tag{2}$$
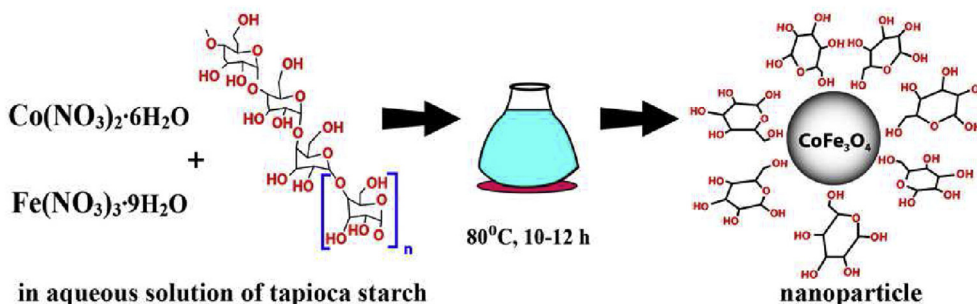

Fig. 1. Schematic of the pristine $CoFe_2O_4$ synthesis using tapioca starch.

Eqs. (3)—(6) were used to calculate the unit cell volume (V), X-ray density (d_x), dislocation density (δ), and hopping lengths in the tetrahedral (L_A) and octahedral sites (L_B) [25].

$$V = a^3 \tag{3}$$

$$d_x = 8M/N^3 \tag{4}$$

$$\delta = 1/D^2 \tag{5}$$

$$L_A = a\sqrt{3}/4; \; L_B = a\sqrt{2}/4 \tag{6}$$

where M denotes the atomic weight and N is Avogadro's number (6.022×10^{23} mol^{-1}). The crystallite size (D) was estimated using Eq. (7) [26]:

$$D = \frac{K\lambda}{\beta \cos\theta} \tag{7}$$

where K, λ, β, and θ denote the shape factor (0.89), X-ray wavelength, full width at the half maximum, and diffraction angle, respectively.

In addition to the D, the lattice strain and defects were influential in the XRD patterns. The Williamson—Hall model is a simplified integral breadth method that separates the contributions from diffraction line broadening. The full width at half maximum of a peak in radians (β_{hkl}) can be expressed as a summation of the contributions from peak broadening by size (β_s) and strain (β_D) in Eq. (8) [27].

$$\beta_{hkl} = \beta_s + \beta_D \tag{8}$$

The Williamson—Hall model assumes uniform strains in all the crystallographic directions. β_{hkl} and θ are related according to Eq. (9).

$$\beta_{hkl} \cdot \cos\theta = 4\epsilon \sin\theta + \frac{K\lambda}{D} \tag{9}$$

The third model, known as the size—strain plot method, is primarily used to account for the isotropic nature of the crystal structure. In this model, the broadening line is non-uniform, and the radiant wavelength regulates the strain size. The profiles of D and size-strain are calibrated using Lorentzian and Gaussian functions, respectively. D and the ϵ parameters are related as shown in Eq. (10).

$$(d_{hkl}\,\beta_{hkl}\cos\theta)^2 = \frac{K}{D\nu}d_{hkl}^2 \cdot \beta_{hkl}\cos\theta + \frac{\epsilon^2}{4} \tag{10}$$

Vibrating sample magnetometry characterizes the magnetic properties of sintered ferrites. An applied magnetic field (H) of up to 10 kOe was scanned at a speed of 10 s/point to trace hysteresis loops at 80 points/loop. Each loop exhibits the coercive field (H_c) and remanent magnetization (M_r) with the saturation magnetization (M_s) approximated using Eq. (11). From these parameters, the magnetocrystalline anisotropy field (H_a), anisotropy constant (K_1), demagnetizing field (H_d), crystalline magnetic moment (μ_{obs}), and squareness were determined using Eqs. 12—16 [28].

$$M = M_s\left(1 - \frac{A}{H} - \frac{B}{H^2}\right) + \chi H \tag{11}$$

$$B = H_a^2/15 \tag{12}$$

$$K_1 = \mu_0 \cdot M_s \sqrt{\frac{105 - B}{8}} \tag{13}$$

$$H_c = 0.48\sqrt{H_a - H_d} \tag{14}$$

$$\mu_{obs} = M \cdot M_s / 5585 \tag{15}$$

$$squareness = M_r/M_s \tag{16}$$

where A, B, and χ are the variables that influence the sample heterogeneity, magnetocrystalline anisotropy, and domain spontaneous behavior, respectively.

3. Results and discussion

3.1. Thermal stability

Based on the TGA curve of pristine $CoFe_2O_4$ (Fig. 2), the decomposition of the dry gel comprises three states. The first significant weight loss from 2 to 9% between 200 and 400 °C corresponds to the removal of physisorbed water molecules and the complex breakdown. The combustion of the hydroxyl groups in the dry gel releases CO_2, H_2O, and
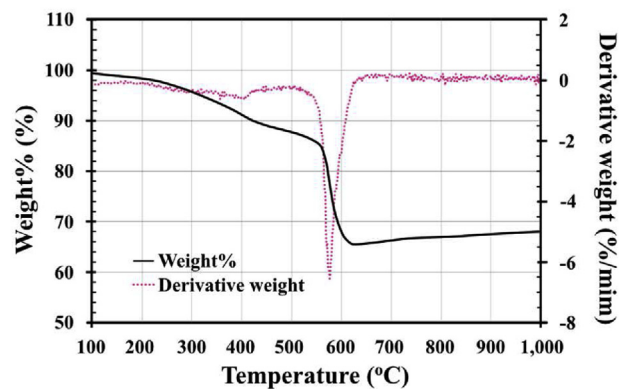
Fig. 2. TGA and DTG curves of the pristine $CoFe_2O_4$.

residues. The combustion of organic compounds occurs in an oxidizing environment [29]. The second weight loss of approximately 10−13% from 420 to 520 °C is owing to the OH group dehydration, forming semi-organic carbon materials and metal oxides [30]. The largest weight reduction from 520 to above 600 °C signifies precursor decomposition and the formation of spinel ferrites.

The third weight loss corresponds to a derivative weight approximately −6%/min in the DTG curve, as shown in Fig. 2. This sharp peak at 576 °C is dependent on the type of material and starch in the sol−gel synthesis because it occurs at a higher temperature than those reported for ZnO synthesis using tapioca starch [20] and the $CoFe_2O_4$ synthesis using sago starch [14]. Above 650 °C, the DTG curve exhibited an insignificant weight change, suggesting that the carbonaceous precursors completely decomposed, and the spinel ferrite phase was completely formed. Therefore, a higher temperature of 800 °C was selected for sintering sol−gel-derived products with ion substitutions to enhance ferrite crystallinity.

3.2. FT-IR spectra

The FT-IR spectrum of each sintered ferrite in Fig. 3 shows the adsorption bands of the three major components. Corresponding to the moisture in the samples, a broad absorption peak at 3446 cm^{-1} indicates the O−H bending in adsorbed water molecules, whereas a small band at approximately 1632 cm^{-1} is in the O−H stretching reg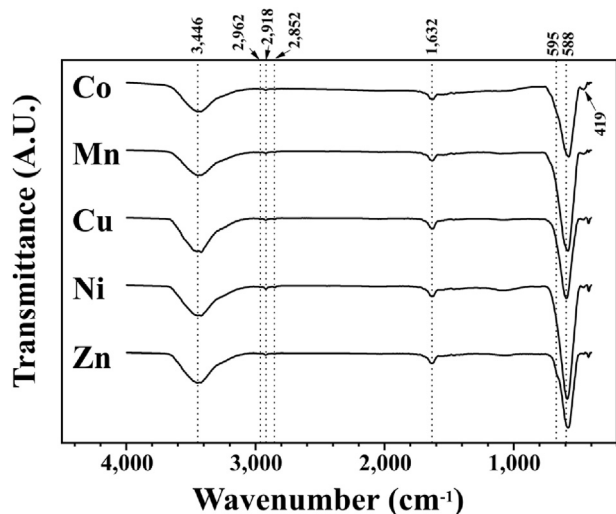ion [31]. The second component is related to the residues of the chelating agent. The triple peaks at approximately 2852, 2918, and 2963 cm^{-1} are ascribed to the anti-symmetric and symmetric stretching of CH_2- and the boundary stretching of C−H, respectively [32,33]. Finally, the sharp peak at 590 cm^{-1} corresponds to the (Fe−O) vibration in the tetrahedral A-site. In contrast, the absorption at 420 cm^{-1} with lower intensity indicates metallic bonds in the octahedral B-site [34]. Furthermore, the absorption peak at 588 cm^{-1} observed exclusively in pristine $CoFe_2O_4$ corresponds to the stretching of Fe−O bonds in the ferric oxyhydroxide (α-FeO(OH)) phase [35].

3.3. Morphology

The SEM micrograph in Fig. 4 reveals nonuniform particles with irregular shapes. The grain size was approximately 20 nm. However, the particles tend to agglomerate into bulky aggregates because of magnetic attraction.

3.4. Crystallographic structure and parameters

The XRD patterns of the sintered ferrites in Fig. 5 exhibit a major characteristic peak corresponding to the (311) crystallographic plane. Other diffractions were from the (220), (222), (400), (422), (511), and (440) planes. These XRD peaks signify cubic spinel $CoFe_2O_4$ (JCPDS card no 22−1086) of the space group Fd3m [36]. In addition, pristine $CoFe_2O_4$ in Fig. 4a exhibits diffraction from the (202) plane. This small XRD peak agrees with the Fe−O stretching in the FT-IR spectra of the tetrahedrally structured α-FeO(OH) phase (JCPDS card no 22−0713) [37]. In contrast, the ion substitutions in Fig. 4b−e did not lead to an impurity phase.
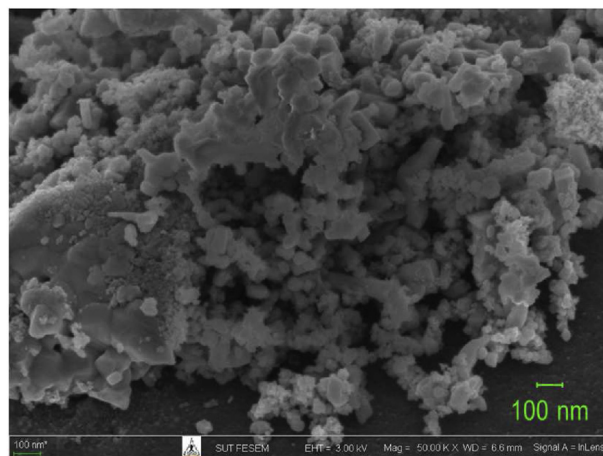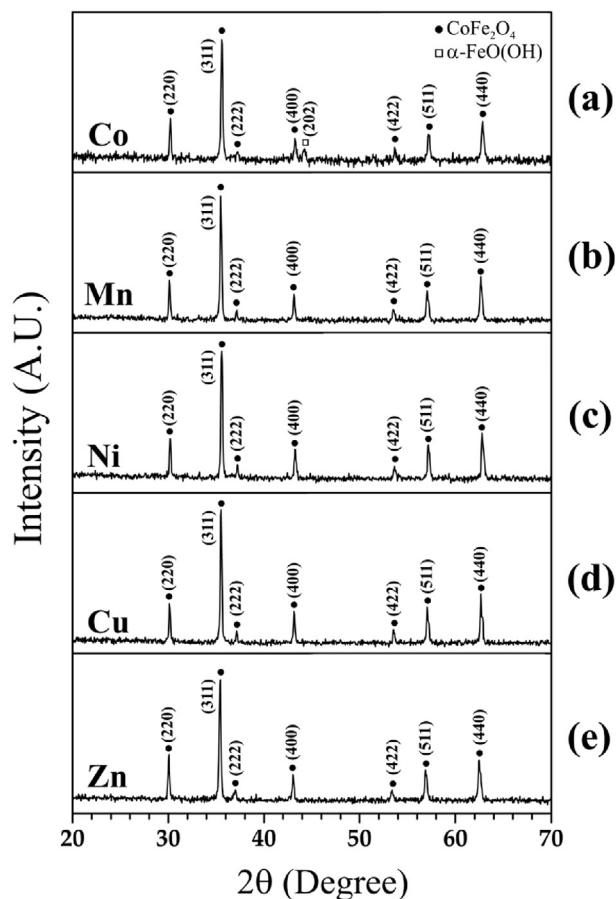

Fig. 3. FT-IR spectra of the $Co_{0.7}Me_{0.3}Fe_2O_4$ samples. Co denotes the pristine $CoFe_2O_4$.

Fig. 4. SEM micrograph of the pristine $CoFe_2O_4$.

Fig. 5. XRD spectra of (a) CoFe₂O₄, (b) Co₀.₇Mn₀.₃Fe₂O₄, (c) Co₀.₇Ni₀.₃Fe₂O₄, (d) Co₀.₇Cu₀.₃Fe₂O₄, and (e) Co₀.₇Zn₀.₃Fe₂O₄.

The corrected lattice constant a was determined by extrapolating the function to zero. The strains within the grains are indicated by the change in a, as shown in Fig. 6. The corrected lattice (a_{co}) parameter
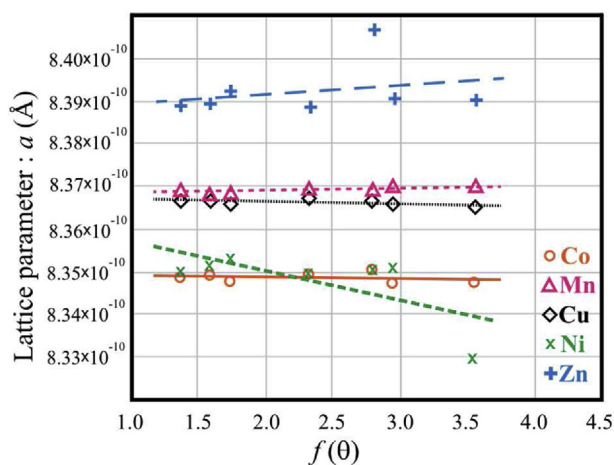

Fig. 6. Nelson–Riley plots for Co₀.₇Me₀.₃Fe₂O₄ samples. Co denotes the pristine CoFe₂O₄.

agreed with our previously uncorrected results. The increase in a_{co} corresponds to the positive slope of the plot between a and $f(\theta)$ for Co₀.₇Mn₀.₃Fe₂O₄ and Co₀.₇Zn₀.₃Fe₂O₄. In these cases, Co²⁺ ions of 0.70 Å in radius are substituted by larger ions, that is, Mn²⁺ (0.83 Å) or Zn²⁺ (0.74 Å) [38]. However, the a_{co} decreased when smaller ions of Cu²⁺ (0.73 Å) and Ni²⁺ (0.69 Å) replaced Co²⁺. Thus, the slope of a versus $f(\theta)$ became negative for Co₀.₇Cu₀.₃Fe₂O₄ and Co₀.₇Ni₀.₃Fe₂O₄.

Table 1 lists the increased crystallographic parameters owing to ion substitutions. Variations in the calculated values from Eqs. (3)−(6) are related to the substitution of ions of different sizes within the CoFe₂O₄ crystal [39]. The a_{co}, V, L_A, and L_B parameters are ranked based on the ionic radius, that is, from Ni²⁺ (0.69 Å), Cu²⁺ (0.73 Å), and Mn²⁺ (0.80 Å), to Zn²⁺ (0.83 Å) [40]. The d_x and δ parameters, which are dependent on M and D, are also influenced by other factors.

3.5. Crystallite size and microstrain

Following the Scherrer equation in Eq. (7), cosθ is plotted versus 1/β on the x-axis in Fig. 7a. D was then derived using the slope of the linear least-squares fit. The extrapolation and slope of the fitted line in Fig. 7b can be used to estimate D and ε based on to the Williamson−Hall model in Eq. (9). For the size-strain model in Eq. (10), the term $(d_{hkl} \cdot \beta_{hkl} \cos\theta)^2$ is plotted versus $d^2_{hkl}\beta_{hkl} \cos\theta$ in Fig. 7c. The slope represented the D parameter and the y-intercept gives the ε.

Table 2 compares the results from the Scherrer, Williamson−Hall, and size−strain plots. The D value obtained from the size-strain model was significantly smaller than those from the other two models. The highest D obtained for CoFe₂O₄ contrasts the others. According to the Scherrer and Williamson−Hall models, CoFe₂O₄ and Co₀.₇Zn₀.₃ Fe₂O₄ have substantially smaller D values. The Williamson−Hall method, providing information on

Table 1. Crystallographic parameters of Co₀.₇Me₀.₃Fe₂O₄ samples. Co denotes the pristine CoFe₂O₄.

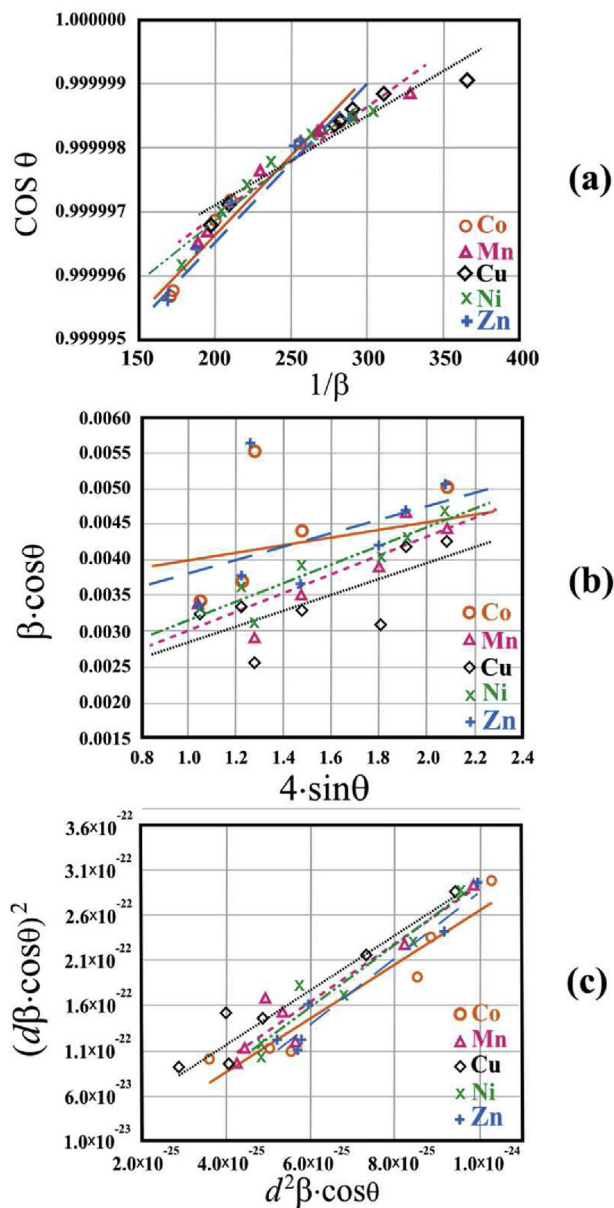| Parameter	Me substitution				
	Co	Mn	Cu	Ni	Zn
a (Å)	8.360	8.374	8.379	8.374	8.391
a_{co} (Å)	8.357	8.380	8.376	8.361	8.401
V (Å³)	583.74	588.47	587.61	584.43	592.86
d_x (gm/cm³)	5.336	5.273	5.332	5.306	5.318
δ (× 10¹⁴ line/m²)	3.513	3.596	3.518	3.551	3.536
L_A	3.619	3.629	3.627	3.620	3.638
L_B	2.955	2.963	2.961	2.956	2.970

Fig. 7. (a) Scherrer, (b) Williamson—Hall, and (c) size—strain plots for $Co_{0.7}Me_{0.3}Fe_2O_4$ samples. Co denotes the pristine $CoFe_2O_4$.

both D and ϵ, suggests that the strains are higher in the case of smaller crystallites. The results do not agree with the size-strain model, with no correlation between D and ϵ.

3.6. Magnetic properties

The pristine $CoFe_2O_4$ and $Co_{0.7}Me_{0.3}Fe_2O_4$ samples exhibit ferrimagnetic hysteresis loops, as shown in Fig. 8. A significant difference is observed in the case of Zn doping. The $Co_{0.7}Zn_{0.3}Fe_2O_4$ sample exhibited characteristics of soft ferrites, as observed from the narrowest loop in Fig. 8. The magnetic parameters of all samples shown in Table 3 can be compared to those of ion-substituted $CoFe_2O_4$ compiled in a review article by Mmelesi et al. [1]. Large M_s and moderate H_c values by Zn substitution have also been reported in the literature using different co-precipitation and solid-state methods. Other substitutions using this tapioca starch sol—gel synthesis led to higher M_s values than those typically obtained in the literature. Compared to our previous study using sago starch with different ratios [14], the M_s values of the pristine samples were comparable at approximately 70 emu/g. The
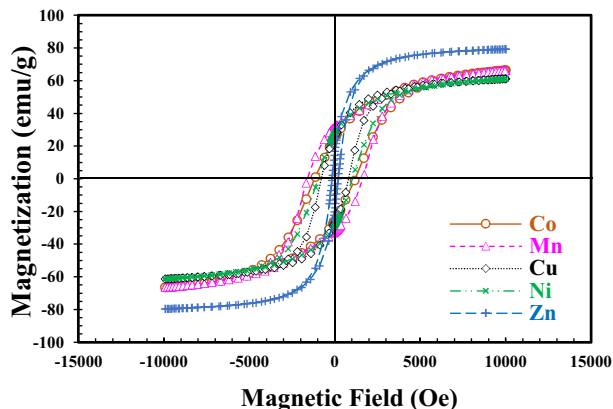
Fig. 8. Hysteresis loops of $Co_{0.7}Me_{0.3}Fe_2O_4$ samples. Co denotes the pristine $CoFe_2O_4$.

Table 2. Crystallite size (D) and effective strain (ϵ) for $Co_{0.7}Me_{0.3}Fe_2O_4$ samples, derived from Scherrer, Williamson—Hall (W—H), and size-strain (SS) plots. Co denotes the pristine $CoFe_2O_4$.

Me	D (nm)			ϵ ($\times 10^{-3}$)	
	Scherrer	W—H	SS	W—H	SS
Co	57.741	42.019	31.599	2.8989	2.2216
Mn	83.179	84.028	29.595	1.7234	1.9982
Cu	102.924	81.276	28.834	1.7818	7.4390
Ni	76.703	77.284	27.103	1.8738	2.8173
Zn	57.695	49.956	26.001	2.8989	3.4514

Table 3. Magnetic parameters of $Co_{0.7}Me_{0.3}Fe_2O_4$ samples. Co denotes the pristine $CoFe_2O_4$.

Parameter	Me substitution				
	Co	Mn	Cu	Ni	Zn
M_s (emu/g)	72.61	72.46	64.98	62.02	83.36
M_r (emu/g)	25.85	32.15	26.45	28.70	17.51
Squareness	0.356	0.4437	0.4070	0.4628	0.2101
H_c (Oe)	1187	1630	796.1	1003	182.1
H_d (Oe)	1884	1936	960.8	476.8	2154
μ_{obs}	2451	3373	1646	2083	357.4
K_1^3 ($\times 10^3$ erg/cm^3)	22.05	22.72	12.57	6.54	21.96

significant differences are the enhanced H_c and the reduced M_r in Table 3.

The M_s values of $CoFe_2O_4$ and $Co_{0.7}Mn_{0.3}Fe_2O_4$ were greater than those of $Co_{0.7}Ni_{0.3}Fe_2O_4$ and $Co_{0.7}Cu_{0.3}Fe_2O_4$, and these results were consistent with those reported by Balakrishnan et al. [41] and Sanpo et al. [42]. By incorporating Co^{2+} (3μ) (d^7) or Mn^{2+} (5μ) (d^5) into the ferrite structure, a larger magnetic moment is incorporated at saturation. M_s is less than 65 emu/g in the case of a lower μ parameter from Cu^{2+} (μ) (d^{10}) or Ni^{2+} (2μ) (d^5) in the crystals. Interestingly, doping with nonmagnetic Zn led to the highest M_s in Table 3. The substitution of magnetic Co^{2+} (μ) by Zn^{2+} (0μ) likely forces Co^{2+} into the A_{tet}-site of the inverse spinel structure. Substantial magnetization then arises from the change in superexchange interactions between the A_{tet}-site and the B_{oct}-site [43]. At the lowest M_r, the $Co_{0.7}Zn_{0.3}Fe_2O_4$ sample exhibited the lowest squareness, as shown in Table 3. The lowest H_c and $μ_{obs}$ values also corresponded to soft ferrite characteristics.

Table 3 summarizes the parameters calculated from Eqs. 12–16. The K_1 and $μ_{obs}$ values exhibit a similar trend to those of M_s, attaining the maximum in $CoFe_2O_4$ and $Co_{0.7}Mn_{0.3}Fe_2O_4$. A smaller μ parameter from either Cu or Ni substitutions reduces K_1 and $μ_{obs}$ values. Although Cu^{2+} has a smaller μ parameter than Ni^{2+}, the crystallites in $Co_{0.7}Cu_{0.3}Fe_2O_4$ are more likely to orient in a preferential direction. H_c is the magnetic field required in the reverse direction to randomize the magnetic moments, whereas the H_d indicates the total magnetic field in a region within the magnetic material. The variations in H_c and H_d in Table 3 can be partially explained using the magnetic moment interaction principle [44]. H_d is directly related to the number of μ occupied, that is, Mn^{2+} (5μ), Co^{2+} (3μ), Ni^{2+} (2μ), Cu^{2+} (μ), and Zn (0μ). In contrast, H_c is significantly influenced by the particle size and microstructure.

4. Conclusions

Divalent ion substitution in sol–gel-derived $Co_{0.7}Me_{0.3}Fe_2O_4$ was achieved using an aqueous solution of tapioca starch as a chelating agent. After sintering at 800 °C for 4 h, the cubic spinel $CoFe_2O_4$ phase without an impurity phase was confirmed by the XRD and FT-IR spectra when Me is Mn, Cu, Ni, or Zn. In addition to suppressing the minor α-FeO(OH) phase, substitution by ions of different sizes modified the lattice parameters according to the Nelson–Riley plots. The Scherrer, Williamson–Hall, and size-strain models were fitted to the XRD data to estimate the crystallite size and microstrain. The Williamson–Hall model yielded smaller D values and higher values for $CoFe_2O_4$ and $Co_{0.7}Zn_{0.3}Fe_2O_4$. The magnetic properties derived from the ferrimagnetic hysteresis loops are sensitive to ion substitutions. $Co_{0.7}Ni_{0.3}Fe_2O_4$ and $Co_{0.7}Cu_{0.3}Fe_2O_4$ exhibited M_s values below 65 emu/g. The substitution by Zn^{2+} substantially increased M_s and reduced H_c. Such soft ferrite characteristics are likely attributed to the relocation of Co^{2+} to the A_{tet}-site after Zn^{2+} is introduced into the inverse spinel structure.

Conflict of interest

The authors declare no conflict of interest.

Acknowledgments

References

[1] O.K. Mmelesi, N. Masunga, A. Kuvarega, T.T. Nkambule, B.B. Mamba, K.K. Kefeni, Cobalt ferrite nanoparticles and nanocomposites: photocatalytic, antimicrobial activity and toxicity in water treatment, Mater Sci Semicond Process. 123 (2021) 105523, https://doi.org/10.1016/j.mssp.2020.105523.

[2] S.Y. Srinivasan, K.M. Paknikar, D. Bodas, V. Gajbhiye, Applications of cobalt ferrite nanoparticles in biomedical nanotechnology, Nanomedicine. 13 (10) (2018) 1221–1238, https://doi.org/10.2217/nnm-2017-0379.

[3] S. Jauhar, J. Kaur, A. Goyal, S. Singhal, Tuning the properties of cobalt ferrite: a road towards diverse applications, RSC Adv. 6 (2016) 97694, https://doi.org/10.1039/C6RA21224G.

[4] D.S. Mathew, R.S. Juang, An overview of the structure and magnetism of spinel ferrite nanoparticles and their synthesis in microemulsions, Chem Eng J. 129 (2007) 51–65, https://doi.org/10.1016/j.cej.2006.11.001.

[5] V. Vaithyanathana, K. Ugendarb, J.A. Chelvanec, K.K. Bharathid, S.S.R. Inbanathan, Structural and magnetic properties of Sn and Ti doped Co ferrite, J Magn Magn Mater. 328 (2015) 88–92, https://doi.org/10.1016/j.jmmm.2015.01.052.

[6] A.A. Rodríguez-Rodríguez, S. Martínez-Montemayor, C.C. Leyva-Porras, F.E. Longoria-Rodríguez, E. Martínez-Guerra, M. Sánchez-Domínguez, $CoFe_2O_4$-TiO_2 hybrid nanomaterials: synthesis approaches based on the oil-in-water microemulsion reaction method, J Nanomater. 2017 (2017) 2567856, https://doi.org/10.1155/2017/2367856.

[7] A.M. Elshahawy, S.A. Makhlouf, Structural and magnetization studies of cobalt ferrite nanoparticles synthesized by the microwave-combustion method, Curr Anal Chem. 14 (2018) 641–645, https://doi.org/10.2174/1573411014666171229162156.

[8] S.M. Montemayor, L.A. García-Cerda, J.R. Torres Lubian, Preparation and characterization of cobalt ferrite by the

polymerized complex method, Mater Lett. 59 (2005) 1056–1060, https://doi.org/10.1016/j.matlet.2004.12.004.

[9] S.E. Shirsath, S.S. Jadhav, M.L. Mane, S. Li, Ferrites obtained by sol–gel method, in: L. Klein, M. Aparicio, A. Jitianu (Eds.), Handbook of sol-gel science and technology, 2nd ed., Springer, International, 2016: pp. 695–735, https://doi.org/10.1007/978-3-319 -32101-1.

[10] P.P. Khirade, Structural, microstructural and magnetic properties of sol-gel-synthesized novel BaZrO$_3$–CoFe$_2$O$_4$ nanocomposite, J Nanostructure Chem. 9 (2019) 163–173, https://doi.org/10.1007/s40097-019-0307-8.

[11] S. Singh, S. Singhal, Transition metal-doped cobalt ferrite nanoparticles: efficient photocatalyst for photodegradation of textile dye, Mater Today Proc. 14 (2019) 453–460, https://doi.org/10.1016/j.matpr.2019.04.168.

[12] C. Brinker, G. Scherer, Sol-gel science-the physics and chemistry of sol-gel processing, 1st ed., Academic Press, Boston, USA, 2013, ISBN 9780121349707.

[13] B.A. Joda, Z.M.A. Al-Kadhim, H.J. Ahmed, A.K.H. Al-Khalaf, A convenient green method to synthesize β-carotene from edible carrot and nanoparticle formation, Karbala Int Mod Sci. 8 (1) (2022) 2, https://doi.org/10.33640/2405-609X.3200.

[14] A. Hunyek, C. Sirisathitkul, C. Mahaphap, U. Boonyang, W. Tangwatanakul, Sago starch: chelating agent in sol-gel synthesis of cobalt ferrite nanoparticles, J Australian Ceram Soc. 53 (2017) 173–176, https://doi.org/10.1007/s41779-017-0022-1.

[15] R.E. Lu, K.G. Chang, B. Fu, Y.J. Shen, M.W. Xu, S. Yang, X.P. Song, M. Liub, Y.D. Yang, Magnetic properties of different CoFe$_2$O$_4$ nanostructures: nanofibers versus nanoparticles, J Mater Chem C. 2 (2014) 8578–8584, https://doi.org/10.1039/C4TC01415D.

[16] A. Hajalilou, S.A. Mazlan, M. Abbasib, H. Lavvafi, Fabrication of spherical CoFe$_2$O$_4$ nanoparticles via sol–gel and hydrothermal methods and investigation of their magnetorheological characteristics, RSC Adv. 6 (2013) 89510–89522, https://doi.org/10.1039/C6RA13493A.

[17] M.S. Hossain, MdB. Alamy, M. Shahjahan, MoH.A. Begum, MdM. Hossain, S. Islam, N. Khatun, M. Hossainz, M.S. Alamy, Md. Al-Mamunx, Synthesis, structural investigation, dielectric and magnetic properties of Zn^{2+}-doped cobalt ferrite by the sol–gel technique, J Adv Dielectr. 8 (2018) 1850030, https://doi.org/10.1142/S2010135X18500303.

[18] C.V. Reddy, C. Byon, B. Narendra, D. Baskar, G. Srinivas, J. Shim, S.V.P. Vattikuti, Investigation of structure, thermal and magnetic properties of cadmium substituted cobalt ferrite nanoparticles, Superlattice Microst. 82 (2015) 165–173, https://doi.org/10.1016/j.spmi.2015.02.014.

[19] U.S. Rashid, S. Simsek, S.R. Kanel, A.N. Bezbaruah, Modifed tapioca starch for iron nanoparticle dispersion in aqueous media: potential uses for environmental remediation, SN Appl Sci. 1 (2019) 1379, https://doi.org/10.1007/s42452-019-1364-9.

[20] W. Lopes de Almeida, F.S. Rodembusch, N.S. Ferreira, V. Caldas de Sousa, Eco-friendly and cost-effective synthesis of ZnO nanopowders by tapioca-assisted sol-gel route, Ceram Int. 46 (2020) 10835–10842, https://doi.org/10.1016/j.ceramint.2020.01.095.

[21] W. Lopes de Almeida, N.S. Ferreira, F.S. Rodembusch, V. Caldas de Sousa, Study of structural and optical properties of ZnO nanoparticles synthesized by an eco-friendly tapioca-assisted route, Mater Chem Phys. 258 (2021) 123926, https://doi.org/10.1016/j.matchemphys.2020.123926.

[22] A. Hunyek, C. Sirisathitkul, P. Harding, Synthesis and characterization of CoFe$_2$O$_4$ particle by PVA sol-gel method, Adv Mater Res. 93 (2010) 659–663, https://doi.org/10.4028/www.scientific.net/AMR.93-94.659.

[23] D. Soundararajan, K.H. Kim, Synthesis of CoFe$_2$O$_4$ Magnetic nanoparticles by thermal decomposition, J Magn. 19 (2014) 5–9, https://doi.org/10.4283/JMAG.2014.19.1.005.

[24] M. Basak, L. Rahman, F. Ahmed, B. Biswas, N. Sharmin, Calcination effect on structural, morphological and magnetic properties of nano-sized CoFe$_2$O$_4$ developed by a simple co-precipitation technique, Mater Chem Phys. 264 (2021) 124442, https://doi.org/10.1016/j.matchemphys.2021.124442.

[25] S. Anand, A.P. Amaliya, M.A. Janifer, S. Pauline, Structural, morphological and dielectric studies of zirconium substituted CoFe$_2$O$_4$ nanoparticles, Mod Electron Mater. 3 (2017) 168173, https://doi.org/10.1016/j.moem.2017.10.001.

[26] S. Mustapha, M.M. Ndamitso, A.S. Abdulkareem, J.O. Tijani, D.T. Shuaib, A.K. Mohammed, A. Sumaila, Comparative study of crystallite size using Williamson-Hall and Debye-Scherrer plots for ZnO nanoparticles, Adv Nat Sci: NanoSci Nanotechnol. 10 (2019) 045013, https://doi.org/10.1088/2043-6254/ab52f7.

[27] V.D. Mote, Y. Purushotham, B.N. Dole, Williamson-Hall analysis in estimation of lattice strain in nanometer-sized ZnO particles, J Theor Appl Phys. 6 (2010) 6, https://doi.org/10.1186/22 51-7235-6-6.

[28] S.E.M. Ghahfarokhi, M. Ahmadi, I. Kazeminezhad, Effects of Bi^{3+} Substitution on structural, morphological, and magnetic properties of cobalt ferrite nanoparticles, J Supercond Nov Magn. 32 (2019) 3251–3263, https://doi.org/10.1007/s10948-019 -5058-8.

[29] R.B. Kamble, V. Varade, K.P. Ramesh, V. Prasad, Domain size correlated magnetic properties and electrical impedance of size dependent nickel ferrite nanoparticles, AIP Adv. 5 (2015) 017119, https://doi.org/10.1063/1.4906101.

[30] M. Sajjia, M. Oubaha, M. Hasanuzzaman, A.G. Olabi, Developments of cobalt ferrite nanoparticles prepared by the so-gel process, Ceram Int. 40 (2014) 1147–1154, https://doi.org/10.1016/j.ceramint.2013.06.116.

[31] W.S. Mohamed, M. Alzaid, M.D.M. Abdelbaky, Z. Amghouz, S. García-Granda, A.M. Abu-Dief, Impact of Co^{2+} substitution on microstructure and magnetic properties of Co$_x$Zn$_{1-x}$Fe$_2$O$_4$ nanoparticles, Nanomaterials. 9 (2019) 1602, https://doi.org/10.3390/nano9111602.

[32] F. Weo, H. Wang, W. Ran, T. Liu, X. Liu, Preparation of S-N co-doped CoFe$_2$O$_4$@rGO@TiO$_2$ nanoparticles and their superior UV-Vis light photocatalytic activities, RSC Adv. 9 (2019) 6152–6162, https://doi.org/10.1039/C8RA10238D.

[33] A. Dey, M.K. Purkait, Effect of fatty acid chain length and concentration on the structural properties of the coated CoFe$_2$O$_4$ nanoparticles, J Ind Eng Chem. 24 (2015) 181–187, https://doi.org/10.1016/j.jiec.2014.09.027.

[34] Y. Chen, C. Zou, M. Mastalerz, S. Hu, C. Gasaway, X. Tao, Applications of micro-Fourier transform infrared spectroscopy (FTIR) in the geological sciences: a review, Int J Mol Sci. 16 (2015) 20223–30250, https://doi.org/10.3390/ijms161226227.

[35] H. Parmar, R. Desai, R.V. Upadhyay, Structural characterization of microwave-synthesized zinc-substituted cobalt ferrite nanoparticles, Appl Phys A. 104 (2011) 229–234, https://doi.org/10.1007/s00339-010-6115-0.

[36] T.J. Castro, S.W. da Silva, F. Nakagomi, N.S. Moura, A. Franco Jr., P.C. Marais, Structural and magnetic properties of ZnO–CoFe$_2$O$_4$ nanocomposites, J Magn Magn Mater. 389 (2015) 27–33, https://doi.org/10.1016/j.jmmm.2015.04.036.

[37] M. Hojamberdiev, G. Zhu, A. Eminov, K. Okada, Template-free hydrothermal synthesis of hollow α-FeOOH urchin-like spheres and their conversion to α-Fe$_2$O$_3$ under low-temperature thermal treatment in air, J Cluster Sci. 24 (2013) 97–106, https://doi.org/10.1007/s10876-012-0522-7.

[38] Periodic table of elements - sorted by ionic radius, Environmental Chemistry com. 1995 - 2021, Available online: https://environmentalchemistry.com/yogi/periodic/ionicradius.html. (Accessed 15 October 2021). accessed on.

[39] T. Dippong, E.A. Levei, I.G. Deac, E. Neag, O. Cadar, Influence of Cu^{2+}, Ni^{2+}, and Zn^{2+} ions doping on the structure, morphology, and magnetic properties of Co-ferrite

embedded in SiO_2 matrix obtained by an innovative sol-gel route, Nanomaterials. 10 (2020) 580, https://doi.org/10.3390/nano10030580.

[40] K. Nadeem, M. Shahid, M. Mumtaz, Competing crystallite size and zinc concentration in silica coated cobalt ferrite nanoparticles, Prog Nat Sci: Mater Int. 24 (2014) 199–204, https://doi.org/10.1016/j.pnsc.2014.05.011.

[41] P. Balakrishnan, P. Veluchamy, Synthesis and characterization of transition metal ions (Zn, Ni, Mn) doped $CoFe_2O_4$ nanoparticles, IOSR J Appl Phys. 8 (5) (2016) 19–29.

[42] N. Sanpo, J. Wang, C.C. Berndt, Sol-gel synthesized copper substituted cobalt ferrite nanoparticles for biomedical applications, J Nano Res. 22 (2013) 95–106, https://doi.org/10.4028/www.scientific.net/JNanoR.25.110.

[43] Y. Chang, J. Shi, Y. Tang, H. Zhang, Z. Yue, W. Yao, Y. Bai, J. Cao, Investigation of significant magnetic transformation for hydrogenated $ZnFe_2O_4$ nanoparticles, J Mater Sci. 55 (2020) 1464–1474, https://doi.org/10.1007/s10853-019-04053-y.

[44] D.D. Ebbing, General chemistry, 5th ed., Houghton Mifflin Company, Boston, USA, 1996, ISBN 0-395-74415-6.